ORIGINAL RESEARCH ARTICLE

Incorporation of Pd Catalyst into Highly Effective Borophene Nanosheet Co-Catalyst for Electrokinetics and Electrochemical Oxygen Reduction Reactions

Wendy Mabhulusa[1] · Kutloano Edward Sekhosana[1] · Xolile Fuku[1]

Abstract

To improve the performance of the system, it is of great importance to develop efficient catalysts for ethanol (EtOH) electro-oxidation. Pd/B electrocatalyst was synthesized using a sonochemical method. Structural and electrochemical properties of the prepared nanomaterial were investigated using electrochemical and physical techniques such as Raman spectroscopy, electrochemical impedance spectroscopy (EIS), x-ray diffraction (XRD), zetersizer, Fourier transform infrared spectroscopy (FTIR), scanning electron microscopy (SEM), high-resolution transmission electron microscopy (HR-TEM) and energy-dispersive x-ray spectroscopy (EDS) and cyclic voltammetry (CV). FTIR confirmed all the functional groups of carbon black, Pd/C, borophene, and Pd/B, and the crystallinity was investigated using XRD. EIS showed that Pd/B has a faster charge transfer and, through investigation using CV, Pd/B showed a more negative onset potential and higher current (-0.76 V vs. Ag|AgCl; 0.07 mA) than Pd/C (-0.65 V vs. Ag|AgCl; 0.05 mA), indicating a more catalytic behavior and tolerance of Pd/B. The active sites could be attributed to the addition of borophene. During the anodic sweeping direction of Pd/B electrocatalyst, it was observed that the ratio of backward peak current (I_{bwd}) to forward peak current (I_{fwd}), (I_{bwd}/I_{fwd}) of in a 2 M of NaOH + 2 M of EtOH is almost equal to (I_{bwd}/I_{fwd}) 1 which shows excellent tolerance of Pd/B to poisoning by ethanol intermediate species. The electron transfer rate (K_s) values for Pd/B at 0.1 M, 0.5 M, 1 M, 1.5 M, and 2 M were estimated to be 4.50×10^{-13} s^{-1}, 1.08×10^{-12} s^{-1}, 4.28×10^{-13} s^{-1}, 5.25×10^{-14} s^{-1} and 9.35×10^{-14} s^{-1}. At 2 M there is a faster electron transfer than at other concentrations which is also evidenced by the obtained diffusion values (D) of the system which were found to be 2.92×10^{-7} cm^2 s^{-1}, 4.72×10^{-8} cm^2 s^{-1}, 4.82×10^{-8} cm^2 s^{-1}, 1.22×10^{-7} cm^2 s^{-1}, and 9.12×10^{-8} cm^2 s^{-1}. The electrochemically active surface area (ECSA) is strongly related to intrinsic activity, Pd/B (1.85 cm^2/mg $\times 10^{-5}$ cm^2/mg) denotes the highest Pd-O stripping charge than Pd/C (1.13 cm^2/mg $\times 10^{-5}$ cm^2/mg).

Keywords Electrocatalyst · Borophene · Performance · Ethanol oxidation · Pd/B

Introduction

Many electrocatalysts have been researched for their potential catalytic properties. The platinum group metals (PGMs), which include palladium and platinum, are mostly utilized as catalysts and are well known for their remarkable qualities, including high activity and selectivity.[1,2] According to Q. Li,[3] metals like Pt and Pd are the most durable and effective catalysts in acidic electrolytes, with an exchange current of approximately 10^{-3} mA/cm^2. According to Ghumnan et al.,[4] Pt demonstrates favorable ethanol oxidizing properties, particularly in an acid media. Palladium (Pd) can be employed as an alternative electrocatalyst since it has characteristics that are similar to those of Pt.[1,5] In alkaline media, palladium (Pd) is a more potent electrochemical oxidation reaction (EOR) catalyst. The broad commercial usage of these materials has been constrained by high cost. To reduce the cost of the PGMs as catalysts, carbon material can be used as a support.[6,7] Carbon materials have been widely researched as electrode materials due to their outstanding physical, and chemical characteristics. Carbon materials have received a lot of attention in recent years due to their availability, physicochemical features, processability, and inexpensive cost.[8,9]

✉ Kutloano Edward Sekhosana
  sekhoke@unisa.ac.za

[1] Institute for Nanotechnology and Water Sustainability (iNanoWS), College of Science, Engineering, and Technology, University of South Africa, Roodepoort 1710, Florida, South Africa

Carbon materials have unique properties that make them attractive materials for use in a wide range of electrochemical applications, including metal refining, electrocatalysis, and fuel cells.[10,11] Additionally, to help reduce catalyst poisoning and the difficulty of breaking the C-C chain in ethanol molecules, which results in poor cell performance functioning, carbon materials are used as a gas diffusion layer, electrocatalyst support, and oxygen reduction reaction (ORR) electrocatalyst.[12,13] When used as a support material for nanoparticles (like Pt), carbon material plays a fundamental role in providing good electrical conductivity with a large surface area, corrosion stability under oxidising conditions, and bringing catalyst particles close to the reactants via the pore structure.[14,15] An electrode with sufficient porosity, good electrical conductivity, and high surface area is desired in order to promote good reactant and high stability in the fuel cell environment.[16,17] However, amorphous carbonaceous materials, when utilized as an electrocatalyst support, exhibit increased oxidation rates at high potentials over time. These drawbacks have prompted extensive research into enhancing amorphous carbon material properties and discovering substitute carbon-based materials for carbon black.[18–20] In this work, borophene (B) nanosheets were used as alternative support material because of their two-dimensional structure and composition involving boron atoms arranged in a hexagonal lattice.[21] Borophene has excellent electrical conductivity and mechanical strength, making it an ideal catalyst for use as a support material.[22] Borophene is not only a good conductor, but also a superconductor of both electricity and heat. It is extremely lightweight but strong, has a high heat conductivity, and is an excellent material for conducting electrons in fuel cells.[23] Borophene is flexible and less expensive.[23] In the current work, the structure and composition of borophene nanosheets were examined using transmission electron microscopy, scanning electron microscopy, Raman spectroscopy, and attenuated total reflection Fourier transform infrared spectroscopy. The electrochemical experiment results show that borophene has good catalytic performance as well as cycling stability.

Experimental

Materials or Reagents and Materials

Palladium on carbon (Pd/C; 10 wt.% loading, matrix activated carbon support), acetone (ACS) reagent ($\geq$ 99.5%), palladium (Pd) powder (submicron < 1 μm, > = 99.9% trace metals basis, palladium, 3 wt.%), carbon black, boron powder, polytetrafluoroethylene (60 wt.% DISPER), absolute ethanol (ISO, $\geq$ 99% (GC)), sodium hydroxide pellets (anhydrous) (grade $\geq$ 98%) were supplied by Merck. All

reagents were of analytical grades and were used without further purification.

Synthesis

Synthesis of Borophene

Free-standing borophene sheets were synthesized by dissolving boron powder (150 mg, 14 mmol) in acetone (40 mL). The beaker was immersed in an S 15 H Elmasonic bath and sonicated for 24 h. The resulting fluids were centrifuged for 6 min at a speed of 4500 rpm to separate out the borophene, which was then removed and dried overnight in the oven at 80℃.

Synthesis of Pd/B

Pd/B nanocomposite was synthesized by dissolving borophene (150 mg, 14 mmol) in 40 mL of acetone. The solution was placed in the S 15 H Elmasonic bath, and the dispersion was ultrasonically treated for 3 h. Palladium powder (20 mg, 0.17 mmol) was then added to the solution, followed by centrifugation of the resultant fluids at a speed of 4500 rpm for 6 min. Pd/B electrocatalyst was collected and dried in an oven for overnight.

Instrumentation

The functional groups of the prepared materials were studied using FTIR spectra and were recorded on a PerkinElmer FT-IR spectrometer Frontier, spotlight 400 with KBr pellet procedure. XRD patterns were recorded on a Rigaku SmartLab x-ray diffractometer with Cu Ka radiation. Scanning electron microscopy (SEM) (JOEL IT 300). The structural morphology of the samples was studied using a JEOL JEM 2100 at 200 kV. A Thermo Fischer detector was used for EDS, and samples were dissolved in ethanol and sonicated for $\pm$ 20 mins and dispersed on a carbon-coated copper grid for analysis. The particle size distribution was determined using the Malvern Zetasizer nano-series (ZS) MAC1129694.

Electrochemical Experiment

All the electrochemical measurements were carried out at room temperature on an EC-lab V11.50 Biologic (Biologic Science Instruments GmbH, Rodeweg 20, D-37081 Gottingen, Germany) with a three-electrode cell comprising of glassy carbon electrode (GCE made from polyetheretherketone (PEEK), diameter: 3 mm; $A = 0.071$ cm^2) as the working electrode, platinum electrode as the counter electrode, and silver-silver chloride (Ag|AgCl) as the reference electrode containing the saturated NaCl solution (~3 M). For typical modification of the electrode, a Pd borophene (Pd/B)

(20 mg) was placed in ethanol (5 mL), and ultrasonicated to form a dark brown homogeneous suspension from which 5 µL was taken and put on a well-polished GCE and dried at 80℃ in an oven, followed by the deposition of Polytetrafluoroethylene (PTFE) (0.05 wt.%) (~10 µL) to fully bind the deposit on the electrode surface. For comparison, a Pd/C-modified electrode was prepared following a similar procedure. The cyclic voltammetric experiments were carried out in an N_2-purged NaOH at different concentrations and NaOH (2 M) containing EtOH (2 M) at different scan rates (10-100 mV s^{-1}) using a potential window of -1 V to $+0.3$ V vs Ag|AgCl unless otherwise specified. The EIS experiments were carried out in NaOH (2 M) alone and when containing EtOH (2 M) at a fixed potential window. All experiments were performed at room temperature.

Results and Discussion

Structural Characterization

The XRD profiles of the electrocatalysts (C, B, Pd/B and Pd/C) were investigated as shown in Fig. 1. The XRD patterns of C, and Pd/C (commercial) catalysts are shown in Fig. 1A and B. The broad peaks found at $2\theta = 10°$, 29°, 26.2° are assigned to the (110), (002), (002) plane of carbon black.

The peaks at $2\theta = 10°$, 29°, 40.1°, and 68° correspond to the (110), (002), (111), (220) plane of face-centered cubic structure of Pd.[24,25]

XRD patterns of the prepared borophene are given in Fig. 1C which describe few-layered borophene at $2\theta = 11°$, 17°, 20. 7°, 31°, and 37°. In line with the planes, the peaks match different phases such as (100), (110), (111), (211), (110).[26,27] Borophene is more prominent with a large sharp peak made of β_{12} and the sharp peak areas signed to the clearer and crystalline structure of borophene. The XRD patterns for Pd/B shown in Fig. 1D are ascribed to 11°, 17°, 40°, 46°, 68°, and 81°, which corresponds to (100), (110), (111), (311), (211), and (311), respectively. All of these reflections are consistent with previous reported observations.[28,29] The addition of Pd to borophene nanosheets results in a drop in peak intensity at 11° and 17°, confirming Pd insertion. Pd, borophene, and carbon black peaks are all present in the patterns, and their shapes and widths are consistent with all XRD patterns.[30,31]

The resulting HR-TEM images provide morphological information of the prepared and the commercial materials. Fig. 1E-H shows the HR-TEM images of the prepared borophene nanosheets, Pd/B, commercial carbon black, and Pd/C, respectively. Fig. 1F shows the HR-TEM images of borophene nanosheets. Fig. 1F exhibits the frees-standing borophene nanosheets. The borophene nanosheets have
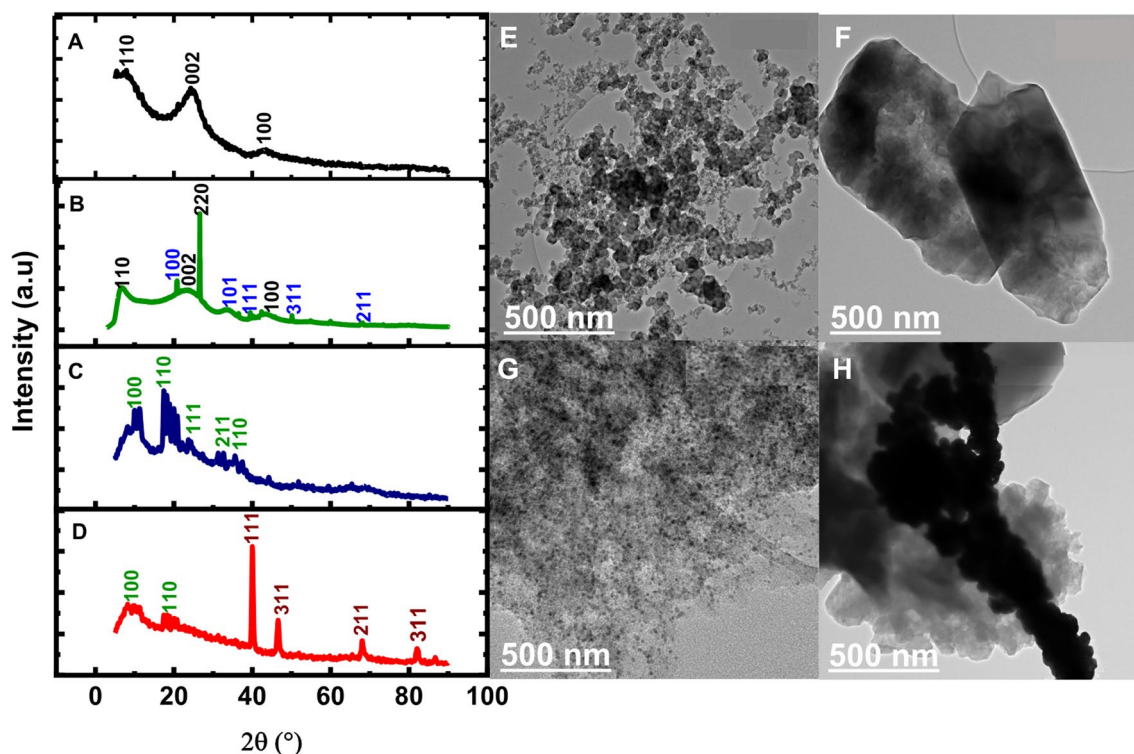

Fig. 1 x-ray diffractograms of (A) Carbon black, (B) Borophene, (C) Pd/C, (D) Pd/B and HR-TEM images of (E) Carbon black, (F) Borophene, (G) Pd/C and (H) Pd/B.

a crystalline structure with a lattice spacing of 0.89 nm. This information is the signature of the β_{12} phase of borophene. The HR-TEM image shown in Fig. 1E indicates the agglomerated state of carbon black. The shape and degree of joined branching of the aggregates is referred to as the structure of carbon black. The structure of carbon black is well-characterized by the arrangement of particles, differences in primary particle size, and aggregate morphology. Fig. 1G shows that the nanoparticles were crystallized and Pd is uniformly dispersed on carbon black. Pd/C has grains in terms of morphology. Pd/B in Fig. 1H revealed differences in the average diameter of the palladium particles and in the particle size distribution. Pd and borophene nearly show the same distribution, indicating that Pd is deposited on the surface of B with large grains as compared to Pd/C in Fig. 1G.

Figure 2 reveals the morphological structures and elemental components of borophene, Pd/C, Pd/B, and powdered carbon black. Disparities in structure and morphology were observed in the SEM images of borophene, Pd/C, Pd/B, and powdered carbon black in Fig. 2 A-D. The conglomerates of borophene nanosheets with varying morphological structures are depicted in Fig. 2A. Both elongated needle- or sheet-like particles and particles with irregular shapes are present in the sample and are comparable to those reported before.[32] A micrograph of carbon black is shown in Fig. 2B where agglomerated imperfections are visible on the surface. The SEM image of Pd/B presented in Fig. 2C comprises small Pd spheres on top of borophene particles that resemble sheet-like assemblies. The formation of the prepared nanocatalyst is confirmed by the different structures. Porous structures with spherical materials exhibit a relatively homogeneous distribution of Pd and grains of carbon black as evidenced by the Pd/C micrographs (Fig. 2D). Figure 2E-H shows the elemental components of the prepared borophene, Pd/B, the commercial carbon black, and Pd/C catalysts. Carbon and boron appear both at 0.5 eV (Fig. E-F), confirming the presence of the carbon and sheet-like materials.[33] Pd is found at 3 eV and 0.5 eV in both the prepared and commercial catalysts (Fig. 2 G-H).

To ascertain the nanosized and polydispersity index (PDI) characteristics of the Pd/B and Pd/C, ZetaSizer average distribution analysis was performed (Table I). Pd/B and Pd/C have average particle size distributions of 505 nm (PDI of 0.403) and 745 nm (PDI of 0.546), respectively. Compared to larger particles, smaller particles have a larger surface area relative to their volume.[11,34] This is because smaller particles have more surface atoms than larger particles, and the surface area of catalyst particles is mostly determined by their external surface. Catalytic activity is frequently enhanced by the larger surface area of smaller catalyst particles and, because there are more active sites per unit area, more molecules of the reactant
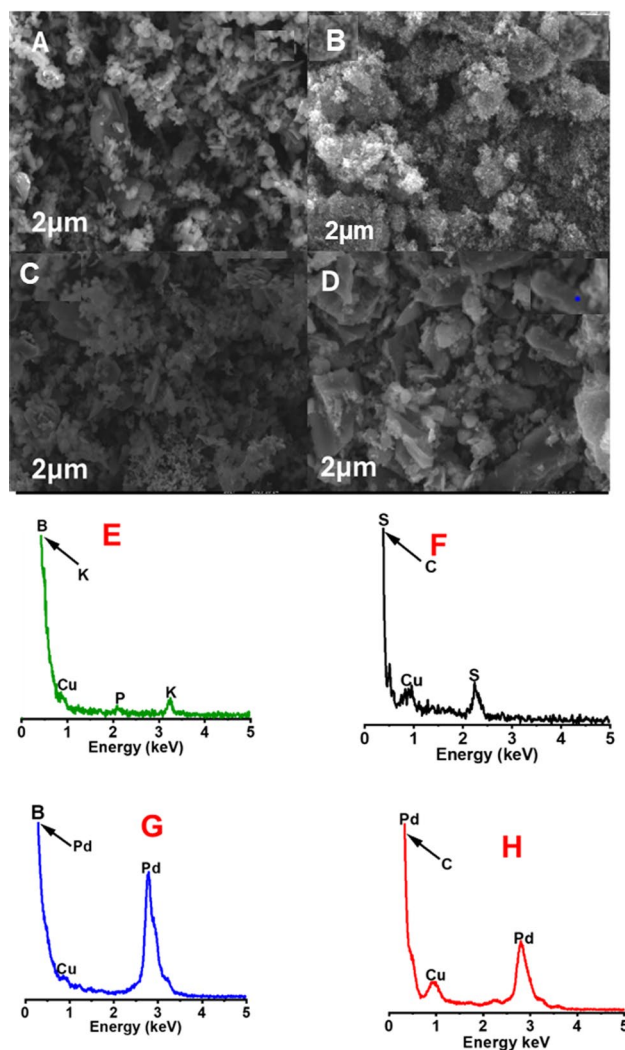

Fig. 2 SEM micrographs of (A) borophene, (B) carbon black, (C) Pd/B, (D) Pd/C and the EDS spectra of (E) carbon black, (F) borophene, (G) Pd/B and (H) Pd/C.

Table I ZitaSizer and HR-TEM Characteristics of nano Pd/B and Pd/C

Catalyst	ZitaSizer		TEM
	Size (nm)	PDI	Size (nm)
Pd/B	505	0.403	500
Pd/C	745	0.546	500

can interact with the catalyst, speeding up and improving the efficiency of the reaction.[35,36] The resultant particle sizes are comparable with those found in HR-TEM and high-resolution scanning electron microscopy (HR-SEM) micrographs.

The FTIR technique was employed to offer additional details regarding the surface functional groups of the carbon
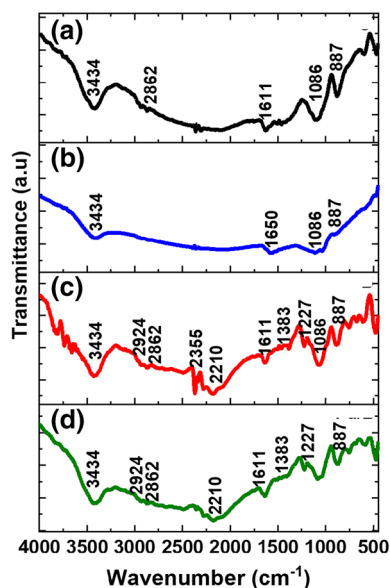
Fig. 3 FTIR spectra of (A) borophene, (B) carbon black, (C) Pd/B, and (D) Pd/C.

Fig. 4 Raman spectra of (A) borophene, (B) carbon black, (C) Pd/C, and (D) Pd/B.

black, Pd/B and commercial Pd/C catalysts, and the prepared borophene (Fig. 3).

The vibrational peaks of carbon black were found at 2862 cm^{-1}, 3434 cm^{-1}, and 887 cm^{-1}, depicting the C-H, O-H and C-H bonds, respectively, as illustrated in Fig. 3A. As can be observed in Fig. 3B, the absorption bands for COO$^-$, C−O, and O−H in the commercial Pd/C were found at 1611 cm^{-1}, 1030 cm^{-1}, and 3434 cm^{-1}. It has been reported that Pd^{2+} adsorption onto the surface of activated carbon can be aided by the functional groups present on the material.[19] It has also been communicated that the synthesized Pd/B could display the same characteristic peaks as those of the commercial Pd/C.[24] The absorption bands of borophene in Fig. 3C were observed at, 3434 cm^{-1} (OH), 2924 cm^{-1} (B-B), 2862 cm^{-1} (B-H), 2355 cm^{-1} (B-H) , 1460 cm^{-1} (B-H), 2210, 1383, 1227 cm^{-1} (B-O), 1650 (B-C), 1067 cm^{-1} (B-O-B), 887 cm^{-1} (C-H), confirming the successful synthesis of borophene.[26,27] The absorption band of the prepared Pd/B were observed at 3434 cm^{-1} (OH), 1030 cm^{-1} (C-O), and 1564 cm^{-1} (COO−), 2924 cm^{-1} (B-B), 2862 cm^{-1} (B−H), 2355 cm^{-1} (B-H), 1227 cm^{-1} (B-O), and 1067 cm^{-1} (B-O-B) as shown in Fig. 3D. The fact that the vibrational peaks of borophene appear on Pd/B suggests that the surface functional group borophene facilitates Pd^{2+} adsorption onto the borophene material.[23,30] In contrast to the Pd/B, borophene showed the absorption peaks at 1460 cm^{-1} (B-H) and 1383 cm^{-1} (B-O). It can, therefore, be concluded that palladium was successfully encapsulated in the borophene as evidenced by the disappearance of the characteristic peaks of borophene and the appearance of characteristic peaks of the palladium on Pd/B.[30]
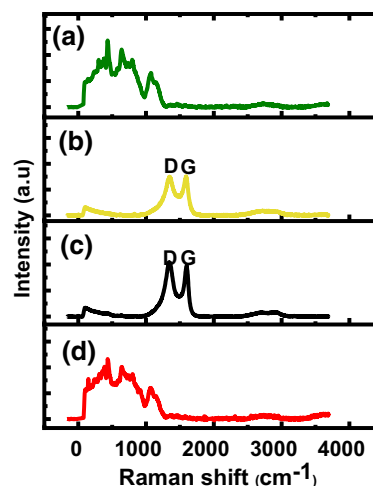
Raman spectroscopy may reveal information about chemical bonds and their vibration modes. Fig. 4A shows Raman spectra with prominent borophene peaks at 467 cm^{-1}, 630 cm^{-1}, 793 cm^{-1}, 811 cm^{-1}, 1083 cm^{-1}, and 1174 cm^{-1}.[21,34] The vibrational modes with wavenumbers 1083 cm^{-1} and 1174 cm^{-1} may be categorized as inter-icosahedral. The modes between 467 cm^{-1} and 811 cm^{-1} are intra-icosahedral.[26,37,38] The Raman spectra of borophene generated by this approach have been verified by the literature,[19,35] and virtually the same trend is found as shown in Fig. 4A. In Fig. 4B and C, the Raman spectra of the carbon black and Pd/C samples displayed characteristic Raman bands, i.e., D (~1340 cm^{-1}) and G (~1590 cm^{-1}) of amorphous carbonaceous material. The defect-induced D-band (disordered carbon) is generated by defects/disorders in the crystalline makeup of the carbon material, whereas the G-band (carbon band) results from the vibrations of the C-to-C bonds. The G band is Raman active in perfect crystalline structures, and the D band only appears in materials with structural defects, disorder, or finite size. ID/IG (intensity ratio of D and G bands) is equal to 1.0, which suggests a high degree of disorder or a substantial density of structural defects in Pd/C and carbon black. Figure 4D shows the borophene peaks and palladium atoms are likely to get entrenched in the borophene matrix, forming nanocrystallites, as determined by XRD and TEM examinations.[33,37]

Electrochemical Performance and Behaviour of the Prepared Catalysts

The Pd/B electrocatalyst activity in a NaOH was examined using the scan rate dependence studies, Fig. 5A-E. The performance and stability of Pd/B were investigated
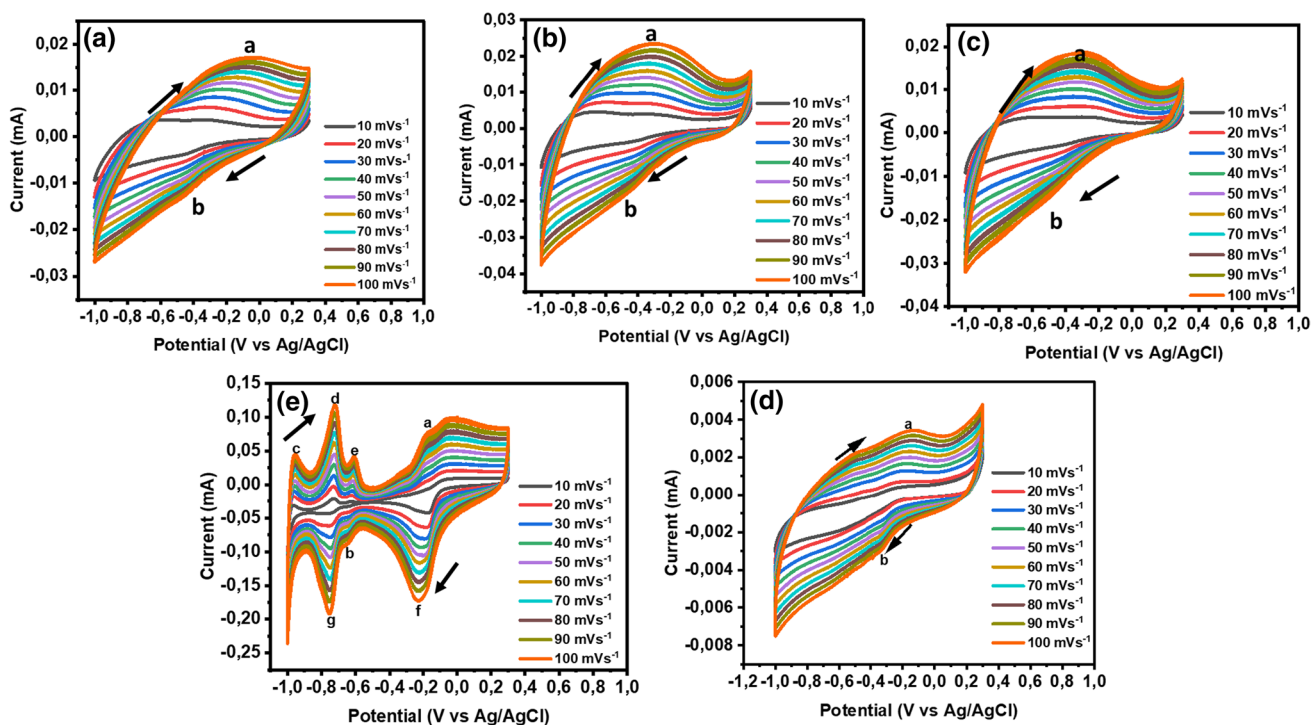
Incorporation of Pd Catalyst into Highly Effective Borophene Nanosheet Co-Catalyst for...

4241

Fig. 5 Scan rate dependent studies of Pd/B at (A) 0.1 M, (B) 0.5 M, (C) 1 M (D) 1.5 (**E**) 2 M of NaOH.
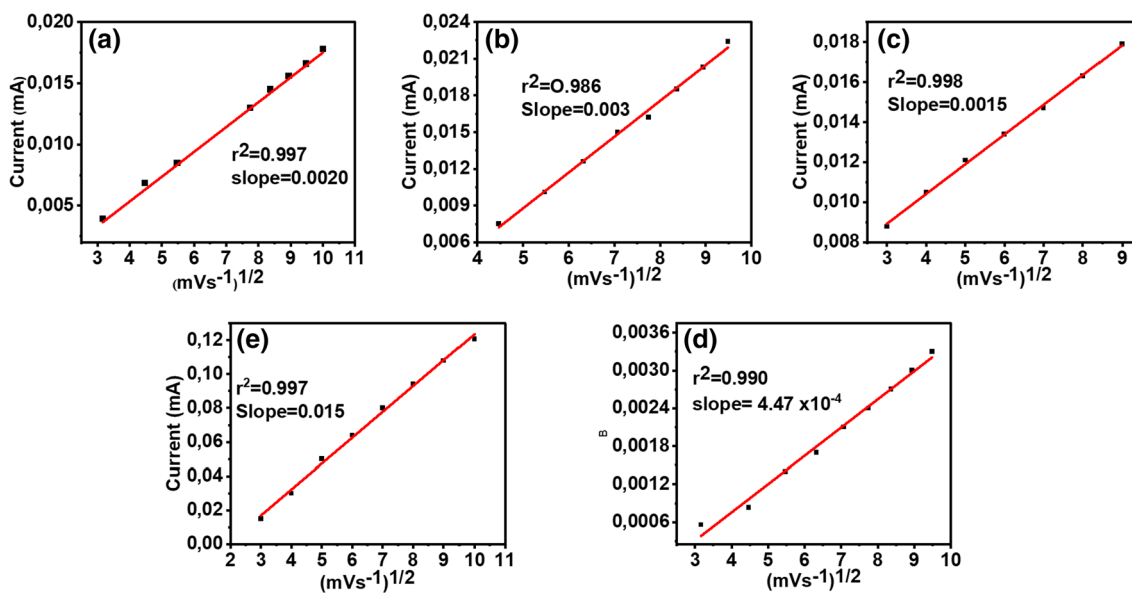

Fig. 6 The current vs root of scan rate of Pd/B at (A) 0.1 M, (B) 0.5 M, (C) 1 M (D) 1.5 M and (E) 2 M NaOH.

by recording all CVs at different scan rates (10 mV s^{-1}, 20 mV s^{-1}, 30 mV s^{-1}, 40 mV s^{-1}, 50 mV s^{-1}, 60 mV s^{-1}, 70 mV s^{-1}, 80 mV s^{-1}, 90 mV s^{-1}, and 100 mV s^{-1}) between -1 V vs Ag|AgCl and 0.3 V vs Ag|AgCl. The electrode current responsiveness was evaluated by changes in anodic

peak currents. It was observed that as the scan rate increases, the oxidation and reduction peaks also increase as shown in Fig. 5A-E. The current was found to increase at 100 mV s^{-1} in response to concentration increases from 0.1 M to 0.5 M (Fig. 5A, B). Conversely, current decreased from 0.5 M to

1 M (Fig. 5A-C), decreased from 1 M to 1.5 M (Fig. 5C-D), and increased from 1.5 M to 2 M (Fig. 5D-E).

It is also illustrated in Fig. 5 that variations in the rate of electrochemical reactions at the electrodes can cause an increase in current when the concentration of an electrolyte solution within an electrochemical cell is increased. The electron transfer rate refers to the speed or rate at which electrons are transferred between species in an electrochemical reaction. This rate is a crucial factor in understanding and characterizing the kinetics of redox reactions occurring at electrode interfaces. The rate of many electrochemical reactions is directly proportional to the reactant concentration.[34] Electron transfer rate is often denoted as K_s as shown in Eq. 1 below:[39]

$$K_s(Ep) = 2.18\left[\frac{D\alpha nFv}{RT}\right]^{1/2} \tag{1}$$

where K_s is the electron transfer rate constant, v the sweep rate, D is the diffusion coefficient, F the faraday's constant, α is the charge transfer coefficient and T is the temperature.

From the Pd oxide peaks at 100 mV/s, the K_s values for Pd/B at 0.1 M, 0.5 M, 1 M, 1.5 M and 2 M were estimated to be 4.50×10^{-13}, 1.08×10^{-12}, 4.28×10^{-13}, 5.25×10^{-14} and 9.35×10^{-14} s^{-1}. At 2 M there is a faster electron transfer than other concentrations. Accordingly, higher reactant concentrations increase the likelihood that reactant molecules will collide with the electrode surface, resulting in faster and more frequent electrochemical reactions.[35] Higher current increases are therefore noted. A potential vs. root of scan rate plot is shown in Fig. 6A-E for the selected scan rates (10 mV s^{-1}, 20 mV s^{-1}, 30 mV s^{-1}, 40 mV s^{-1}, 50 mV s^{-1}, 60 mV s^{-1}, 70 mV s^{-1}, 80 mV s^{-1}, 90 mV s^{-1}, and 100 mV s^{-1}). Peak current increases with the square root of scan rate, indicating the existence of a

diffusion-controlled electrocatalytic process.[40] The findings are in agreement with the results obtained in Fig. 5.

The anodic peak current ($I_{p,a}$) of 0.1 M, 0.5 M, 1 M, 1.5 M and 2 M vs square root of the scan rate show more linear regions. Similar results have been reported by Hu et al.[41] who ascribe these results to the rate-determining steps of Pd oxidation involving both adsorption and diffusion controlled system. The $I_{p,a}$ of 2 M is linearly dependent on the square root of the scan rate, indicating that Pd oxidation is under diffusion control.[28,42] The slopes of Pd/B at 0.1 M, 0.5 M, 1 M, 1.5 M and 2 M (Fig. 6A-E were found to be 0.002 mA, 0.003 mA, 0.0023 mA, 0.000191 mA, and 0.021 mA (V^{-1} s)$^{1/2}$. Pd/B at a 2 M has a larger absolute value (0.021) of the slope as compared to other concentration. The slope of the voltammogram is an important parameter that reflects the sensitivity of the electrode to changes in potential and current, providing insights into the responsiveness of the system to variations in experimental conditions. The slope of a plot is related to the sensitivity of the electrode to changes in concentration. The slope at 2 M is steeper than other concentrations, implying the electrode sensitivity to changes in potential and current with rapid kinetics. A high sensitivity means that the electrode is responsive to small changes in the experimental conditions. The slope may also suggest that Pd oxidation is under diffusion-controlled electrochemical process with $r^2 = 0.997$, and the obtained diffusion values (D) of the system were found to be 2.92×10^{-7}, 4.72×10^{-8}, 4.82×10^{-8}, 1.22×10^{-7}, and 9.12×10^{-8} cm^{2}s^{-1}. The diffusion coefficient was determine using the following equation (Eq. 2):[43]

$$I_p = 2.69 \times 10^5 n^{3/2} A D^{1/2} V^{1/2} C \tag{2}$$

where I_p is the peak current, n is the number of electron transfer, D is the diffusion coefficient, v is the rate at which potential is scanned (scan rate in mV s^{-1}), C is the
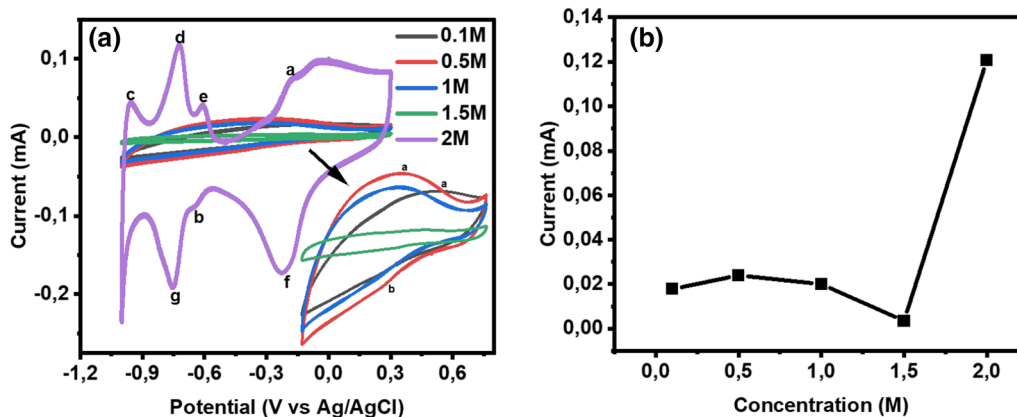

Fig. 7 (A) Concentration dependent studies at 100 mV s^{-1} and (B) The current vs concentration of Pd/B at 0.1 M, 0.5 M, 1 M, 1.5 and 2 M of NaOH.

Table II Shows the peak potential and concentration

Peak potential (V)	Concentration (M)
−0.05	0.1
−0.31	0.5
−0.3	1
−0.12	1.5
−0.2	2

Fig. 8 Cyclic voltammograms of Pd/B and Pd/C (insert) showing the forward potential scans (denoted by peaks a, c, d and e), and the backward potential scans (denoted by peaks b, f and g) in 2 M NaOH at 100 mVs^{-1}.

concentration in mol cm^{-3}. The stability of electrocatalysts is demonstrated by the increase in peak current with the square root of the scan rate.[41] It is important to note that the relationship between concentration and current may not be linear, it depends on the specific electrochemical system and the nature of the reactions involved. This can be due to interactions between ions, ion pairing, or other complexities in the electrochemical system. If the actual reaction involves multiple steps or has a more complex mechanism, the concentration-current relationship may deviate from linearity. Additionally, there may be limits to how much increasing concentration can increase the current.[16,43] When increasing the concentration, the change in the electrochemical behaviour of the electrode surface was affected, which led to the non-linear reaction kinetics as shown in Fig. 6.[19] The peak potential depends on the concentration, at lower concentrations, the surface of the catalyst may not be fully covered with active sites, resulting in lower performance and shifts in the peak potential as shown in Table II.

To examine the Pd/B electrocatalyst activity at various NaOH concentrations, cyclic voltammetry measurements were used, Fig. 7A. The optimal concentration of the catalyst is determined by concentration studies, and this is crucial because utilising a catalyst at an incorrect concentration could result in an undesirable by-product and reduce catalytic activity at the electrode interface.[44–46] The stability of the catalyst can also be ascertained with the aid of concentration studies. Understanding that some catalysts may deteriorate or lose their efficacy at high concentrations or under particular environmental conditions is crucial for long-term catalyst performance.[16]

The performance of the catalyst was evaluated by introducing the Pd/B electrode into 0.1 M, 0.5 M, 1 M, 1.5 M, and 2 M of NaOH under an inert atmosphere. Fig. 7A shows CVs measured at 100 mV s^{-1} between −1 V and 0.3 V vs Ag|AgCl. The current increased as the concentration increased from 0.1 M to 0.5 M but decreased as the concentration increased from 1 M to 1.5 M (Fig. 7B). In comparison to other concentrations (0.1 M, 0.5 M, 1 M, and 1.5 M), it was found that Pd/B behaves better in 2 M of NaOH. The metal oxide (Pd oxide) formation and characteristic peaks are clearly visible in 2 M of NaOH, and
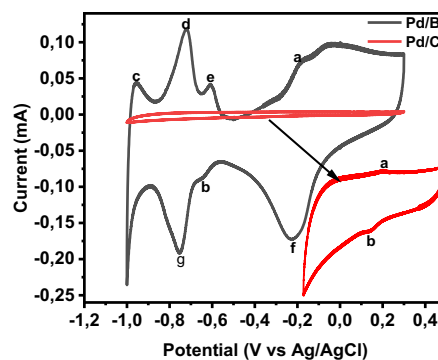
the newly formed oxidation and reduction peaks verify that Pd is present on the surface of an electrode.[41] Surface coverage (Γ) was calculated using Eq. 3:[47]

$$\Gamma = Q/nFA \qquad (3)$$

where Γ is the surface coverage, Q is the charge transfer (C), n number of electron transfers, Faraday's constant (96485°C/mol), and A is the active area of the electrode (cm^2). Γ values were established as 2.92×10^{-10}, 4.72×10^{-11}, 4.82×10^{-11}, 1.22×10^{-10}, and 9.12×10^{-11} cm^2 s^{-1} at 0.1 M to 2 M. The latter finding may be attributed that the surface coverage is directly proportional to the concentration and the electrochemical reaction at 2 M occurs on the Pd/B double layer. In a diffusion-controlled system, the concentration of adsorbed species affects the exchange current which is proportional to K_s. In adsorption-controlled systems, the surface coverage is directly linked to the adsorption and desorption processes, which, in turn, influence the electron transfer rate constants.

The performance of Pd/C-commercial catalyst, and Pd/B catalyst, were compared using cyclic voltammetry measurements at 2 M of NaOH. Pd/C has previously been studied at low concentrations and different scan rates as reported in the literature shows; thus, in this work, Pd/C is only studied at 2 M of NaOH.[34,41,44] The performance of Pd/B, and Pd/C was evaluated at a fixed scan rate of 100 mVs^{-1} and at a potential window of − 1 V to 0.3 V vs Ag|AgCl (Fig. 8).

In the forward potential scan (peak a), there is an oxidation of Pd around (− 0.6 V to − 0.2 V) which is mainly related to palladium oxide oxidation (PdO).[34,48] The reduction of the oxide is produced at the cathodic peak (peak b) around − 0.6 V vs Ag|AgCl. The peak corresponds to the palladium oxide reduction. The prominent peaks were observed at $E_{1pa} = -0.182$ V vs Ag|AgCl (oxidation, peak a), $E_{1pa} = -0.606$ Ag|AgCl (oxidation, peak e) and at $E_{1pa} = -0.225$ V vs Ag|AgCl (reduction, peak f) which is attributed to Pd-O/Pd-OH at 100 mVs^{-1}. The peaks at − 1 V

to -0.67 V vs Ag|AgCl (peak c, and d,) potential region of forward scan as well as reverse scan (peak g) are assigned to the underpotential deposition of hydrogen (H_{upd}) as a result of adsorption/desorption processes. H_{upd} regions also confirms possible differences in the hydrogen adsorption/desorption processes, which can be associated with the distinctions in the structural and crystallographic characteristics of dissimilar surfaces of the Pd catalysts supported on borophene. During the process of anodic scan, the CVs exhibit a broad oxidation peak b, and e of Pd-O/Pd-OH.[49–51] The diffusion coefficients obtained for Pd/B were found to be 9.12×10^{-8} cm^2 s^{-1}, which is substantially higher than that of Pd/C (1.02×10^{-4} cm^{2}s^{-1}) value.

This claims that Pd/B has fast charge transfer than Pd/C. To evaluate other parameter such as activity of the of catalyst, ECSA was calculated. ECSA is the fraction of an electrode's surface where electron transfer reactions occur during electrochemical processes. This parameter (ECSA) was calculated using Eq. 4 [52] to assess the efficiency and electrochemical activity of an electrode by quantifying the available surface area for redox reactions. The ECSA is a key metric in evaluating the performance of electrochemical devices, as it provides insights into the electrode's ability to facilitate electron transfer and influences overall device efficiency.

$$\text{ECSA} = \frac{Q}{(m \times 420)}, \tag{4}$$

where Q is a charge of PdO desorption electrooxidation, m is the total amount of metal on the surface of the electrode, and 420 is the total charge required to oxidize a monolayer of adsorbed PdO on a catalyst surface. ECSA is strongly related to intrinsic activity because it directly influences the number of active sites available for electrochemical reactions. While intrinsic activity reflects the inherent catalytic properties of the material, ECSA provides a measure of the surface area where these intrinsic activities can manifest. Pd/B (1.85×10^{-5} cm^2/mg) denotes the highest Pd-O stripping charge and more active sites available for the oxidation reaction than Pd/C (1.13×10^{-5} cm^2/mg)

EIS measurements were carried out to estimate the electro-kinetics of the used catalysts. The electrochemical impendence spectrum (EIS) was performed at a frequency of 10 mHz to 50 kHz to investigate the charge transport kinetics of Pd/B and Pd/C electrodes. Fig. 9 demonstrates the Nyquist plots of the commercial (Pd/C) and the prepared Pd/B catalysts. Plots in the linear area of EIS correspond to ion diffusion in the electrolyte. Pd/B plot slope is steeper than Pd/C because Pd/B has faster ion diffusion within the electrodes in the redox process with better capacitive behaviour. The results are consistent with a CV diffusional controlled process. When compared to Pd/C (12.73 kΩ), Pd/B (7.32 kΩ) has a smaller semicircle, denoting a lower electron
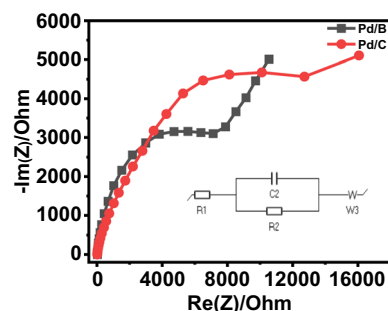
Fig. 9 Nyquist plot of Pd/B and Pd/C at 2 M NaOH.

Table III Rct of Pd/B at different concentrations of NaOH

Rct (kΩ)	Concentration (M)
17.3	0.1
20.9	0.5
12.9	1
9.5	1.5
7.3	2

charge transfer resistance/polarization resistance (R_{ct}/R_p). The results also suggest a higher activity for EOR at the electrode interface. These EIS present a strong agreement with the results obtained from the CVs (Fig. 8) where Pd/B exhibited higher peak current for EOR.

The maximum phase angle ($\omega_{\theta max}$) is used to calculate the double-layer capacitance which is expressed in the following Eq. 5:[47]

$$\omega_{\theta\,max} = \left(1 + \frac{1 + \frac{R_{ct}}{R_{sol}}}{R_{ct}D_{cl}}\right), \tag{5}$$

where R_{sol} is the solution resistance, R_{ct} is the charge-transfer resistance, and is the D_{cl} double layer capacitance.

The Randles Sevcik equivalent circuit (insert, Fig. 9) was used to evaluate the parameters such as R_{sol}, R_{ct}, and Warburg diffusion impedance/mass transfer (W) as evidenced by EIS profiles. The depressed arcs for both electrode samples revealed slow mass transfers (Warburg diffusion) but faster electron kinetics which can be related to oxygen adsorption. The above-mentioned parameters are calculated as shown in Table III. The small semicircle in the Nyquist plot in the high-frequency region is due to double layer capacitance between the electrode interface and electrolyte denoted as R_s. R_{ct} is related to reaction kinetic, and it can be observed that Pd/B has a smaller R_{ct} compared to Pd/C which suggests a faster electron transfer and higher activity for EOR. The R_{ct} value for Pd/B suggests that Pd/B is more of a conducting

system than Pd/C. Additionally, the rate of electron transfer during ethanol oxidation on the Pd surface is slow hence a larger R_{ct}. These EIS results have a strong agreement with results obtained from the CVs where Pd/B exhibited higher peak current for EOR, also, the decrease in Rct and higher phase angle of Pd/B are attributed to higher conductivity and electrocatalytic activity and make it a good candidate for electron transfer reactions (Table IV).

Figure 10 represent the EI spectroscopy of the Pd/C-commercial and Pd/B prepared catalysts at different concentrations of NaOH. The electrochemical impedance spectroscopy (EIS) showed an electron charge transfer resistance at different concentration of NaOH for Pd/B when subjected to a fixed potential of −0.188 V, −0.695 V, −0.7807 V, 0.142 V and −0.483 V vs Ag|AgCl at 0.1 M, 0.5 M, 1 M, 1.5 M and 2 M. When compared to the other concentrations, the Pd/B catalyst at 2 M has a lower resistance which makes the electron-transfer kinetics process quicker and more appropriate for electrocatalytic activities. At high concentration, a decrease in R_{ct} (Table III) indicates that the charge transfer reactions at the electrode-electrolyte interface are occurring at a faster rate. This is often associated with increased reaction kinetics.[42,47] In practise, this means that the electrochemical reactions occur at a faster rate, resulting in faster electrode processes. Reduced charge transfer resistance implies lower energy losses and higher device efficiency.

Investigation of Processes Associated with the Electro-Oxidation of Ethanol

The catalysts activity of Pd/B, and Pd/C were tested in 2 M of NaOH + 2 M EtOH at 100 mV s⁻¹. The catalysts were evaluated for the oxidation of ethanol in an alkaline medium (Fig. 11). During the process of anodic and cathodic scan, the CVs exhibited a broad peak at −0.31 V vs Ag|AgCl (peak a') and −0.22 V vs Ag|AgCl (peak b') of Pd-O for the Pd/B. Voltammograms recorded under conditions of positive (anodic) scan depict a more negative onset of oxidation potentials (−0.23 V vs Ag|AgCl) meaning that less energy is required for the EOR to occur on Pd/B than on Pd/C. Peak a' can also be ascribed to the process of Pd-OH formation.[28,53] Pd/C catalyst has an anodic peak current which is observed at −0.134 V vs Ag|AgCl and is assigned to the Pd-O

oxidation. During the anodic sweeping direction of Pd/B electrocatalyst, it was observed from the ratio of backward peak current (I_{bwd}) to forward peak current (I_{fwd}), (I_{bwd}/I_{fwd}) of Pd/B in NaOH + EtOH is almost equal to (I_{bwd}/I_{fwd}) 1.0 which shows excellent tolerance of Pd/B to poisoning by ethanol intermediate species. This was attributed to the addition of Pd to the surface of borophene. Borophene, serving as a support, significantly facilitated the completion of the oxidation process while concurrently rendering the catalyst resilient against poisoning by intermediate species.[54,55] In comparison to Pd/B, Pd/C had a relatively low peak ratio (I_{bwd}/I_{fwd}) of 0.8, indicating that the catalyst is susceptible to poisoning at the electrode interface. The onset potentials for the ethanol oxidation on the Pd/C and Pd/B catalysts are 0.65 V vs Ag|AgCl and 0.76 V vs Ag|AgCl. Pd/B has a more negative onset potential compared to Pd/C meaning that less energy is required for the EOR to occur on Pd/B than on Pd/C.

Figure 12 depicts the scan rate dependent studies of Pd/B and the corresponding linear plot (inserted) at 2 M NaOH + EtOH for the selected scan rates (10 mV s⁻¹, 20 mV s⁻¹, 30 mV s⁻¹, 40 mV s⁻¹, 50 mV s⁻¹, 60 mV s⁻¹,
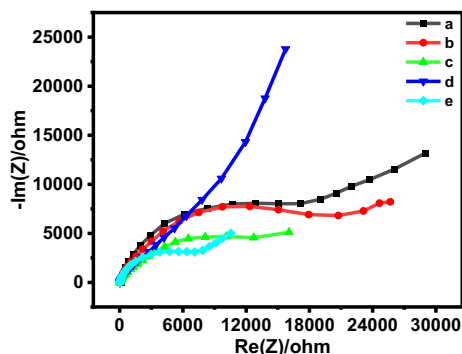
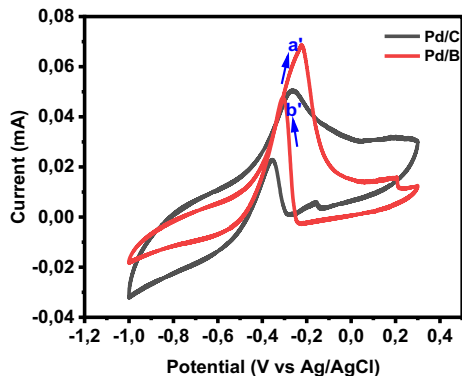**Fig. 10** Nyquist plot of Pd/B at (a) 0.1 M, (b) 0.5 M, (c) 1 M (d) 1.5, (e) 2 M of NaOH.

Fig. 11 CV voltammograms of Pd/B and Pd/C in 2 M NaOH at 100 mVs⁻¹.

Table IV Electrochemical parameters obtained from the electrochemical impedance spectroscopy for Pd/B and Pd/C at 2 M of NaOH.

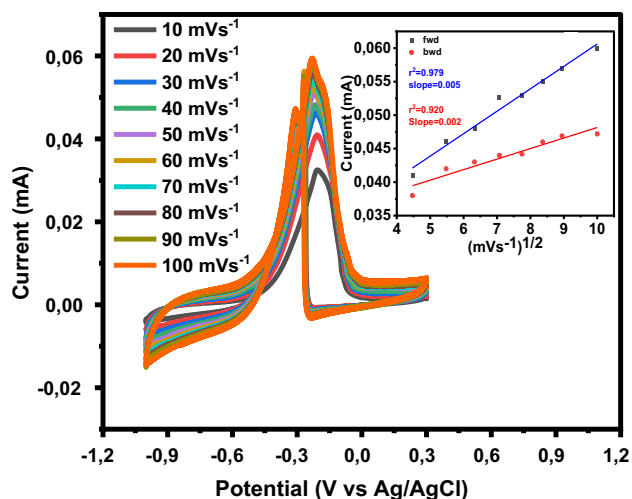| Catalyst	R_{ct} (ohm)	R_s (ohm)	$\omega_{\theta max}$	Phase angle (deg)	Frequency (Hz)
Pd/B	1x10³	100	68.53	72.47	172
Pd/C	1x10⁶	100	242	67	254.8

Fig. 12 The scan rate dependent studies of Pd/B in 2 M NaOH + EtOH and the current vs square root of the scan rate (insert) for both the first and second oxidation processes, respectively.

70 mV s^{-1}, 80 mV s^{-1}, 90 mV s^{-1}, and 100 mV s^{-1}). The electrode current responsiveness was measured using changes in anodic peak currents. The forward (oxidation) peak current and the reduction peak current increased as the scan rate increases. The variation in anodic and cathodic peak currents was used to evaluate electrode current responsiveness. The increase in peak current with the square root of the scan rate as shown by the insert demonstrates the stability of electrocatalysts, revealing a diffusion-controlled electrocatalytic process with $r^2_{\text{fwd}} = 0.979$ (oxidation) $r^2_{\text{bwd}} = 0.920$ (reduction) and the slope of 0.005 for the forward peak and 0.002 for the reverse peak. The steeper slope for the forward peak indicates that the electrode is sensitive to changes in current and potential at high reaction rates. To substantiate the electron's mobility in the system, the diffusion coefficient (D) was calculated for the oxidation and the reverse peak. The obtained diffusion coefficient for the system was found to be 3.96×10^{-4} cm^2 s^{-1} for the oxidation and 3.3×10^{-7} cm^2 s^{-1} for the reduction. The oxidation reaction produced a greater diffusion coefficient, which corresponds to quicker rates of diffusion for the oxidation.

The electrical properties of electrochemical systems were studied using EIS. The semicircle corresponding to the Pd/C electrode catalyst is bigger than that recorded for the Pd/B as shown in Fig. 13. Pd/B exhibits a small semicircle and possesses a lower electron transfer resistance compared with Pd/C. The Pd/B possesses a lower R$_{ct}$ compared to Pd/C which enhances the electron-transfer kinetics process as a faster one and more suitable for the electrocatalytic activities.[47,56] Pd/B shows the smallest diameter on impedance arc, with R$_{ct}$ = 7.15 KΩ indicating the smallest transfer resistance,[49,50] which makes it a better electrocatalyst than

Pd/C at 18.3 KΩ (Table V) with the $\Gamma = 6.64 \times 10^{-11}$ mol/cm^2.

The Randles-Sevcik equivalent circuit is used to fit and simulate the electrochemical parameters. It can be observed that Pd/B has a smaller R_{ct} compared to Pd/C thin film which suggests a faster electron transfer and higher activity for EOR. Also, the decrease in R_{ct} and higher phase angle of Pd/B are attributed to higher conductivity and electrocatalytic activity and make it a good candidate for electron transfer reactions. The narrow semicircle in the high-frequency area of the Nyquist plot is due to double-layer capacitance between the electrode interface and electrolyte, represented as R_s in Table V. Pd/B exhibits an increased phase angle than Pd/C, which might be ascribed to stronger electron conductivity, which is then connected with rapid electron kinetic transfer for EOR. These findings are consistent with the CV findings.

Stability Studies of the Prepared Catalysts

The stability of Pd/B was tested for EOR (2 M of NaOH + 2 M EtOH), the stability of electrocatalysts was tested using CV by running 50 circles at a fixed scan rate (100 mV s^{-1}). The results showed a high but fixed current response for Pd/B throughout the cycling. The higher current response of Pd/B (Fig. 14A) as compared to that of Pd/C (Fig. 14B) is ascribed to available active sites of the
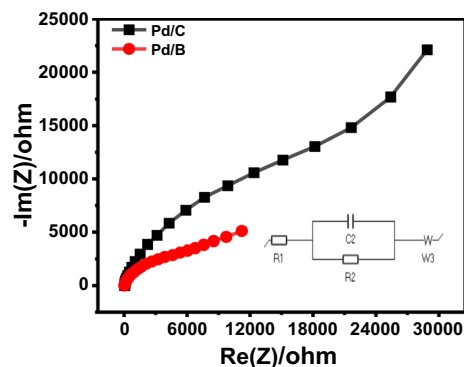

Fig. 13 Nyquist plots generated for electrode catalysts in a solution of 2 M of NaOH + EtOH.

Table V Summarized EIS findings for the performance of Pd/C and Pd/B.

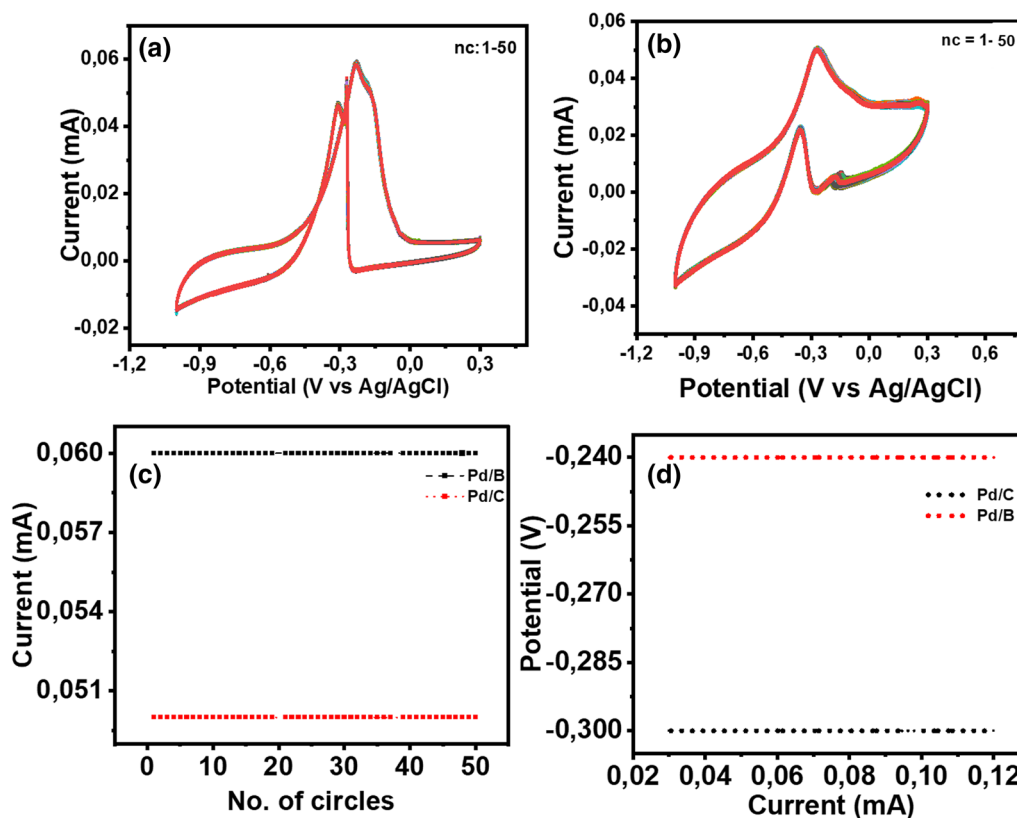| Samples	R_{ct} (ohm)	R_s (ohm)	$\omega_{\theta\max}$	Phase angle (deg)	Frequency (Hz)
Pd/B	7.5	100	68.53	70	90
Pd/C	18.3	100	–	68.9	253

Fig. 14 Current vs potential stability studies of (A)Pd/B, and (B)Pd/C and current vs No. of circles of (C) Pd/B and (D) Pd/C in a 2 M of NaOH + EtOH at 100 mV s^{-1}.

electrocatalyst. This observation corroborates the CV results (Fig. 11) where Pd/B is shown to be more tolerant to the poisoning of the electrocatalyst. Monitoring the stability of the current response over a series of cycles (50 cycles) at a fixed scan rate (100 mV/s) is a key aspect of assessing the reliability and durability of an electrochemical system. The peak current vs the number of circles confirms the stability of electrocatalysts (Fig. 14C). Figure 14D the durability and stability were further tested by plotting the change in potential vs current and the results were compared with Fig. 14C, the results are in agreement. Pd/B showed higher (0.6 mA) current and stability towards ethanol oxidation than Pd/C. This means that the electrochemical active surface and functionality of the electrode material was maintained and there was a consistent electron transfer and reliable current response on the electrode.

Conclusion

Pd/B was synthesized in an ultrasonic water bath at room temperature, with the crystal structure and surface morphology studied using XRD, SEM and HR-TEM. It has been found in this study that Pd/B is capable of reducing the cost of the electrocatalysts used for the oxidation of ethanol when compared to the commercial Pd/C catalyst. Pd/B electrocatalyst demonstrated an increase in the electrochemical oxidation and better durability in a 2 M of NaOH + EtOH. As compared to Pd/C, Pd/B had a higher current density in 2 M of NaOH and 2 M of NaOH + EtOH. Pd/B showed the smallest diameter on impedance arc, with $R_{ct} = 7.15$ KΩ indicating the minimal hinderance in the transfer resistance, which makes it a better electrocatalyst than Pd/C. An improvement of the Pd/B electrocatalytic activity capability was studied by optimizing the concentration of NaOH. The CV results also confirmed that Pd/B showed a more negative onset potential and higher current (−0.76 V vs Ag|AgCl; 0.07 mA) than Pd/C (−0.65 V vs Ag|AgCl; 0.05 mA), indicating a more catalytic behavior and tolerance of Pd/B, with the active sites attributed to the addition of borophene. It was found that the prepared Pd/B electrocatalyst could enhance the electrocatalytic activity towards EtOH. Therefore, it could be pointed out that the interaction between Pd and borophene nanosheets significantly improved the EtOH electrooxidation performance with high current density and extended stability.

Conflict of interest Authors declare no conflict of interest.

References

1. H. Wang, Y. Cao, J. Li, J. Yu, H. Gao, Y. Zhao, Y.U. Kwon, and G. Li, Preparation of Ni/NiO-C catalyst with nio crystal: catalytic performance and mechanism for ethanol oxidation in alkaline solution. *Ionics* 24, 2745 (2018).

2. A. Pareek, R. Dom, J. Gupta, J. Chandran, V. Adepu, and P.H. Borse, Materials science for energy technologies insights into renewable hydrogen energy: recent advances and prospects. *Mater. Sci. Energy Technol.* 3, 319 (2020).

3. W.J. Zhou, B. Zhou, W.Z. Li, Z.H. Zhou, S.Q. Song, G.Q. Sun, Q. Xin, S. Douvartzides, M. Goula, and P. Tsiakaras, Performance comparison of low-temperature direct alcohol fuel cells with different anode catalysts. *J. Power. Sources* 126, 16 (2004).

4. A. Ghumman, C. Vink, O. Yepez, and P.G. Pickup, Continuous monitoring of CO_2 yields from electrochemical oxidation of ethanol: catalyst, current density and temperature effects. *J. Power. Sources* 177, 71 (2008).

5. P. Geng, E. Cao, Q. Tan, and L. Wei, Effects of alternative fuels on the combustion characteristics and emission products from diesel engines: a review. *Renew. Sustain. Energy Rev.* 71, 523 (2017).

6. F. An, X.Q. Bao, X.Y. Deng, Z.Z. Ma, and X.G. Wang, Carbon-based metal-free oxygen reduction reaction electrocatalysts: past, present and future, xinxing tan cailiao/new carbon mater. *J. Power. Sources* 37, 338 (2022).

7. A. Marinoiu, M. Raceanu, E. Carcadea, and M. Varlam, Nitrogen-doped graphene oxide as efficient metal-free electrocatalyst in PEM fuel cells. *Nanomaterials* 13, 1233 (2023).

8. D.W. Lee, M.H. Jin, Y.J. Lee, J.H. Park, C.B. Lee, and J.S. Park, Reducing-agent-free instant synthesis of carbon-supported pd catalysts in a green leidenfrost droplet reactor and catalytic activity in formic acid dehydrogenation. *Sci. Rep.* 6, 1 (2016).

9. A.K. Roy and C.-T. Hsieh, Pulse microwave-assisted synthesis of Pt nanoparticles onto carbon nanotubes as electrocatalysts for proton exchange membrane fuel cells. *Electrochim. Acta* 87, 63 (2013).

10. F.M. Souza et al., The effect of support on Pd1Nb1 electrocatalysts for ethanol fuel cells. *Renew. Energy* 150, 293 (2020).

11. C. Liu, T. Wu, F. Zeng, X. Pan, G. Li, K. Teng, X. Ran, and Q. Qu, Electrochimica acta high-selective and effective carbon nanotubes

12. S. Hanif, N. Iqbal, X. Shi, T. Noor, G. Ali, and A.M. Kannan, NiCo–N-doped carbon nanotubes based cathode catalyst for alkaline membrane fuel cell. *Renew. Energy* 154, 508 (2020).

13. W. He, T. Liu, W. Ming, Z. Li, J. Du, X. Li, and X. Guo, Progress in prediction of remaining useful life of hydrogen fuel cells based on deep learning restricted boltzmann machine. *Renew. Sustain. Energy Rev.* 192, 114193 (2024).

14. A. Nouralishahi, A.M. Rashidi, Y. Mortazavi, A.A. Khodadadi, and M. Choolaei, Enhanced methanol electro-oxidation reaction on Pt-CoOx/MWCNTs hybrid electro-catalyst. *Appl. Surf. Sci.* 335, 55 (2015).

15. S.I.S. Mashuri et al., Photocatalysis for organic wastewater treatment: from the basis to current challenges for society. *Catalysts* 10, 1 (2020).

16. J. Singh, M. Kumar, A. Sharma, G. Pandey, K. Chae, and S. Lee, We are intechopen, the world's leading publisher of open access books built by scientists, for scientists top 1%. *INTECH* 11, 13 (2016).

17. F. Cai, and X. Lei, TM-N4C (TM = Co, Pd, Pt and Ru) as OER electrocatalysts in lithium-oxygen batteries: first-principles study. *Appl. Surf. Sci.* 609, 155331 (2023).

18. H.R. Abbasi, A. Yavarinasab, and S. Roohbakhsh, Waste heat management of direct carbon fuel cell with advanced supercritical carbon dioxide power cycle: a thermodynamic-electrochemical modeling approach. *J. CO2 Util.* 51, 101630 (2021).

19. A.B. Stambouli, Fuel cells: the expectations for an environmental-friendly and sustainable source of energy, renew. *Sustain. Energy Rev.* 15, 4507 (2011).

20. X. Yang, Y. Chen, C. Zhang, G. Duan, and S. Jiang, Electrospun carbon nanofibers and their reinforced composites: preparation, modification, applications, and perspectives. *Compos. Part B* 249, 110386 (2023).

21. M. Ou, X. Wang, L. Yu, C. Liu, W. Tao, X. Ji, and L. Mei, The emergence and evolution of borophene. *Adv. Sci.* 8, 2001801 (2021).

22. B. Kiraly, X. Liu, L. Wang, Z. Zhang, A.J. Mannix, B.L. Fisher, B.I. Yakobson, M.C. Hersam, and N.P. Guisinger, Borophene synthesis on Au(111). *ACS Nano* 13, 3816 (2019).

23. O. Folorunso, Y. Hamam, R. Sadiku, S.S. Ray, and G.J. Adekoya, Synthesis methods of borophene, graphene-loaded polypyrrole nanocomposites and their benefits for energy storage applications: a brief overview. *FlatChem* 26, 100211 (2021).

24. Z. Bin, C. Xueshan, X. Jiaojiao, and Z. Cunshan, Alkaline ionic liquid modified pd/c catalyst as an efficient catalyst for oxidation of 5-hydroxymethylfurfural. *J. Chem.* 2018, 1 (2018).

25. A. Raveendran, M. Chandran, S. Mohammad Wabaidur, M. Ataul Islam, R. Dhanusuraman, and V.K. Ponnusamy, Facile electro-chemical fabrication of nickel-coated polydiphenylamine (Ni/PDPA) nanocomposite material as efficient anode catalyst for direct alcohol fuel cell application. *Fuel* 324, 124424 (2022).

26. S. Güngör, C. Taşaltın, İ Gürol, G. Baytemir, S. Karakuş, and N. Taşaltın, Copper phthalocyanine-borophene nanocomposite-based non-enzymatic electrochemical urea biosensor. *Appl. Phys. A Mater. Sci. Process.* 128, 89 (2022).

27. C. Taşaltın, T.A. Türkmen, N. Taşaltın, and S. Karakuş, Highly sensitive non-enzymatic electrochemical glucose biosensor based on pani: β12 borophene. *J. Mater. Sci. Mater. Electron.* 32, 10750 (2021).

28. X. Fuku, M. Modibedi, N. Matinise, P. Mokoena, N. Xaba, and M. Mathe, Single step synthesis of bio-inspired nio/c as pd support catalyst for dual application: alkaline direct ethanol fuel cell and CO_2 electro-reduction. *J. Colloid Interface Sci.* 545, 138 (2019).

29. C. Mahendiran, T. Maiyalagan, K. Scott, and A. Gedanken, Synthesis of a carbon-coated NiO/MgO core/shell nanocomposite as

a pd electro-catalyst support for ethanol oxidation, mater. *Chem. Phys.* 128, 341 (2011).

30. M.A. Chowdhury, M.M.K. Uddin, M.B.A. Shuvho, M. Rana, and N. Hossain, A novel temperature dependent method for borophene synthesis. *Appl. Surf. Sci. Adv.* 11, 100308 (2022).

31. X. Zhang, Z. Xia, H. Li, S. Yu, S. Wang, and G. Sun, Structure evolution and durability of metal-nitrogen-carbon (M = Co, Ru, Rh, Pd, Ir) based oxygen evolution reaction electrocatalyst: a theoretical study. *J. Colloid Interface Sci.* 640, 170 (2023).

32. E.A. Lebedeva, S.A. Astaf, and T.S. Istomina, modification of boron powders used in energy-saturated materials. *Russ. J. Phys. Chem. B* 16, 316 (2022).

33. C. Shen, E. Barrios, M. McInnis, J. Zuyus, and L. Zhai, Fabrication of graphene aerogels with heavily loaded metallic nanoparticles. *Micromachines* 8, 47 (2017).

34. V. Kumar, P. Wen, F. Lin, A.E. Russell, D.J.L. Brett, and C. Hardacre, Effect of mass transport on the electrochemical oxidation of alcohols over electrodeposited film and carbon-supported pt electrodes. *Top. Catal.* 61, 240 (2018).

35. B. Dhlamini, H.K. Paumo, L. Katata-Seru, and F.R. Kutu, Sulphate-supplemented npk nanofertilizer and its effect on maize growth, mater. *Res. Express* 7, 095011 (2020).

36. Y. Duo, Z. Xie, L. Wang, N. Mahmood Abbasi, T. Yang, Z. Li, G. Hu, and H. Zhang, Borophene-based biomedical applications: status and future challenges. *Coord. Chem. Rev.* 427, 213549 (2021).

37. G. Parakhonskiy, N. Dubrovinskaia, L. Dubrovinsky, S. Mondal, and S. Van Smaalen, High pressure synthesis of single crystals of α-boron. *J. Cryst. Growth* 321, 162 (2011).

38. J. Qin, T. Irifune, H. Dekura, H. Ohfuji, N. Nishiyama, L. Lei, and T. Shinmei, Phase relations in boron at pressures up to 18 Gpa and temperatures up to 2200°C. *Phys. Rev. B Condens. Matter. Mater. Phys.* 85, 2 (2012).

39. L. Cui, G. Lv, and X. He, Enhanced oxygen reduction performance by novel pyridine substituent groups of iron (ii) phthalocyanine with graphene composite. *J. Power. Sources* 282, 9 (2015).

40. J.R.N. dos Santos, I.C.B. Alves, A.L.B. Marques, and E.P. Marques, Ni-Ag supported on reduced graphene oxide as efficient electrocatalyst for alcohol oxidation reactions. *Electrocatalysis* 13, 713 (2022).

41. C.C. Hu and T.C. Wen, Voltammetric investigation of palladium oxides-ii. their formation/reduction behaviour during glucose oxidation in NaOH. *Electrochim. Acta* 39, 2763 (1994).

42. J. Wang, H.B. Sun, S.A. Shah, C. Liu, G.Y. Zhang, Z. Li, and M. Han, Palladium nanoparticles supported by three-dimensional freestanding electrodes for high-performance methanol electro-oxidation. *Int. J. Hydrog. Energy* 45(19), 11089–11096 (2020).

43. L.L. Sikeyi, T.D. Ntuli, T.H. Mongwe, N.W. Maxakato, E. Carleschi, B.P. Doyle, N.J. Coville, and M.S. Maubane-nkadimeng, sciencedirect microwave assisted synthesis of nitrogen doped and oxygen functionalized carbon nano onions supported palladium nanoparticles as hybrid anodic electrocatalysts for direct alkaline ethanol fuel cells. *Int. J. Hydrog. Energy* 46, 10862 (2021).

44. M.A.F. Akhairi and S.K. Kamarudin, Catalysts in direct ethanol fuel cell (DEFC). *Int. J. Hydrog. Energy* 41, 4214 (2016).

45. J. Lilloja et al., Transition-metal- and nitrogen-doped carbide-derived carbon/carbon nanotube composites as cathode catalysts for anion-exchange membrane fuel cells. *ACS Catal.* 11, 1920 (2021).

46. L. Ma, D. Chu, and R. Chen, Comparison of ethanol electro-oxidation on pt/c and pd/c catalysts in alkaline media. *Int. J. Hydrog. Energy* 37, 11185 (2012).

47. A. Mkhohlakali, X. Fuku, M.H. Seo, M. Modibedi, L. Khotseng, and M. Mathe, Electro-design of bimetallic pdte electrocatalyst for ethanol oxidation: combined experimental approach and ab initio density functional theory (DFT)—based study. *Nanomaterials* 12, 3607 (2022).

48. F.A. Zakil, S.K. Kamarudin, and S. Basri, Modified nafion membranes for direct alcohol fuel cells: an overview. *Renew. Sustain. Energy Rev.* 65, 841 (2016).

49. J.A. Arminio-Ravelo and M. Escudero-Escribano, Strategies toward the sustainable electrochemical oxidation of methane to methanol. *Curr. Opin. Green Sustain. Chem.* 30, 100489 (2021).

50. E. Berretti et al., Platinum group metal-free fe-based (Fe[Sbnd]N[Sbnd]C) oxygen reduction electrocatalysts for direct alcohol fuel cells. *Curr. Opin. Electrochem.* 29, 100756 (2021).

51. M. Duraisamy, and E. Mari, Sciencedirect novel palladium-decorated molybdenum carbide/polyaniline nanohybrid material as superior electrocatalyst for fuel cell application. *Int. J. Hydrog. Energy* 47, 37599 (2021).

52. P. Chandran, A. Ghosh, and S. Ramaprabhu, High-performance platinum-free oxygen reduction reaction and hydrogen oxidation reaction catalyst in polymer electrolyte membrane fuel cell. *Sci. Rep.* 8, 1 (2018).

53. M.Z.F. Kamarudin, S.K. Kamarudin, M.S. Masdar, and W.R.W. Daud, Review: direct ethanol fuel cells. *Int. J. Hydrog. Energy* 38, 9438 (2012).

54. Y.S. Li and T.S. Zhao, A passive anion-exchange membrane direct ethanol fuel cell stack and its applications. *Int. J. Hydrog. Energy* 41, 20336 (2016).

55. Y. Chen, Z. Xu, J. Wang, P.D. Lund, Y. Han, and T. Cheng, Multi-objective optimization of an integrated energy system against energy, supply-demand matching and exergo-environmental cost over the whole life-cycle. *Energy Convers. Manag.* 254, 115203 (2022).

56. H. Hou, G. Sun, R. He, Z. Wu, and B. Sun, Alkali doped poly-benzimidazole membrane for high performance alkaline direct ethanol fuel cell. *J. Power. Sources* 182, 95 (2008).